Enhanced photosensing by Mg-doped ZnO hexagonal rods via a feasible chemical route

Published: 12 February 2021

Volume 32, pages 6475–6486, (2021) Cite this article

Journal of Materials Science: Materials in Electronics

Aims and scope

Submit manuscript

Vishnu V. Kutwade, Ketan P. Gattu, Avinash S. Dive, Makrand E. Sonawane, Dipak A. Tonpe & Ramphal Sharma

Abstract

One-Dimensional (1D) pure-ZnO, $Zn_{0.9}Mg_{0.1}O$ and $Zn_{0.8}Mg_{0.2}O$ thin films have been successfully grown over a glass substrate using simple economical chemical bath deposition method (CBD). This investigation explores the enhancement in photocurrent and photosensitivity of $Zn_{1-x}Mg_xO$ thin films via induced defects with vertically aligned hexagonal

rod-like array thin films. The structural, optical and electrical properties of the synthesized materials have been elucidated using X-ray Diffraction (XRD), Raman, UV–Vis spectroscopy, Photoluminescence (PL), and *I*–V characteristics. Hexagonal rod-like morphology has been confirmed from both XRD and SEM results. Change in structural properties revealed that the formation of the $Mg(OH)_2$ phase for $Zn_{1-x}Mg_xO$ thin films from XRD spectra. Thus, the impact of extra Magnesium (Mg) which is difficult to incorporate in ZnO lattice sites which causes the phase segregation and possibly creates morphological and structural defects. This has been also confirmed from electron–phonon interaction in Raman analysis. Such as the Raman-shift of E2 (high) mode in $Zn_{1-x}Mg_xO$ thin films towards higher frequencies indicates the substitution of Mg at O lattice sites. However the formation of phase segregation had a significant effect on optical as well as electrical properties of the ZnO hexagonal rods thin films. From UV–Vis spectra, the intensity of absorption edges for Mg-doped samples are decreases while the optical band gaps are increases from 2.87 to 3.47 eV and also from PL spectrum shows that the defect states in visible range are increases with increasing Mg content in ZnO. The parameters like photocurrent and electrical resistance are calculated from *I*–*V* characteristics and the results shows that the photosensitivity enhanced as Mg content increases in ZnO.

1 Introduction

Photosensors/detectors are sensors that have been able to produce photocurrent (electric current) from absorbed photon energy (solar irradiation) and are among the most prominent elements of contemporary day instruments in daily usage of modern world. They currently exist in diverse technological applications which utilize in various fields such as commerce, entertainment and research. Resultantly, photosensors make a major contribution in manufacturing, automation and robotic application due to flexible advantages. Primary photosensors are the photodiodes which convert absorbed light into an electrical current in a small amount that would be useful to functionalize the circuitry such as motors, actuators, indicators and drivers. Pertinent wavelengths such as infrared, visible and UV are most also targeted by photosensors, which is highly useful if a sensor is used in an area that could be exposed to mass quantities of lighting conditions which would otherwise interfere with the sensor. Visible light sensors (VLS) are useful as an indoor motion and movement tracing sensors. VLS is also getting attention due to its superior properties such as using it will cut down building wiring overheads because it can utilize existing lighting infrastructure as transmitters and it does not penetrate walls. In addition to this, not suffering from radio interference and high sensitivity for small objects and motions arousing by its wavelengths in nanometer scale are its major advantages over RF techniques. Besides VLS remains stable along wide range of temperature. There are several large semiconducting nanomaterials including, InSe [1], CdS [2], CdSe [3], MoS_2 [4], Nb_2O_5 [5], Ga_2O_3 [6, 7], Zn_2GeO_4 [8], Zn_2SnO_4 [9], TiO_2 [10], ZnO [11,12,13,14], NiO [15], CeO_2 [16], V_2O_5 [17], SnO_2 [18], and $K_2Nb_8O_{21}$ [19], have been explored for photosensor/detectors applications. Among these materials, semiconductors of metal oxide (MO) might cover the manufacturing process of a suitable photosensor/detector that satisfies the criteria of high-temperature conditions for the manufacture of devices and freedom in the design of materials [20]. MO semiconductors in nanostructure form have advantages such as they are best for tuning material properties due to higher degree of freedom. The improvement of the spectral response of photodetectors (extended photo-detection of wavelengths) would expand their area of application in visible light. In this regard, past few years, MO semiconductor has gained substantial attention; as we

can easily manipulate optical properties of nanostructured MO semiconductor materials to detect UV and visible spectrum. To achieve UV and visible-light photodetection capability, these are doped with metals [21, 22], non-metals [23], other materials/functional groups are added [24]. The morphology of these materials also plays an important role in the application of photosensing, the one-dimensional (1D) nanostructures show better efficiency in the photo-detection application due to their large surface-to-volume ratio and Debye length [25].

Among the MO semiconductor materials, ZnO is found to be one of the most promising materials for photosensing applications. Due to its many peculiar features viz., wide direct bandgap, *n*-type semiconducting behavior, high tunability of charge carriers, carrier mobility, eco-friendly, low cost, and stability which are attractive characteristics for photosensing applications [12]. Also, ZnO has a wurtzite (hexagonal) crystal structure that is thermodynamically more stable phase at ambient pressure and temperature than the other two crystal structures i.e. zinc blende and rock salt. ZnO nanomaterials are found in different dimensional structures within the range 0 to 3D for promising nanoscale applications. 1D ZnO nanostructures including nanowires (NWs) [26], nanorods (NRs) [27], and nanobelts (NBs) [28] were mostly studied with various modifications to improve the performance of photosensors. In the last few years, as they have excellent optoelectronic properties, one-dimensional nanorods with a columnar form have received great interest [29]. Parameters such as length and width are in several micrometers and nanometers, respectively, which propagate charge carriers freely only along one-dimension. Semiconductor nanorods can sustain high thermal expansion coefficients and lattice mismatches between the nanorods and the substrate as they have strong strain tolerance [30]. Typically, in the dopant/s modifications used, implement their bandgap tuning and defects resulting in the generation of charge carriers following visible-light irradiation resulting in material sensitive to visible light. Fubo et al. (2014), has theoretically investigated MgO–ZnO alloys in details enthalpy calculations and ordered structure using ab initio evolutionary simulations [31]. Xiaojing et al. (2015) elucidate the CaO–ZnO alloys under high pressure, based on the enthalpy calculations they investigated the phase diagram and ab initio evaluationary algorithm embedded USPEX code for the crystal structure [32]. Liriano et al. (2014), ZnO alloys with MgO for the bandgap engineering; their structural and optoelectronic properties were elucidated [33].

Till date, various deposition techniques are used for deposition of ZnMgO thin films but the

chemical routes are low-cost and easy to operate. The work discussed herein elucidated the defects created after Mg-doping and their effect on the enhancement photosensing activities of ZnO under the solar simulator instrument [34]. The 1D Mg-doped ZnO hexagonal rods thin films were successfully synthesized via low-cost chemical bath deposition (CBD) technique [35]. The synthesized Mg-doped ZnO thin films are characterized; such as their crystal structure, morphological, and electron–phonon interaction. While the electronic properties were discussed with the tuning of bandgap and deep level defects generated in ZnO thin films; characterized by UV–Vis spectroscopy and photoluminescence studies. At last we have discussed in details the photosensing mechanism for synthesized Mg-doped ZnO and also the photosensing with response and recovery time using $J-V$ characteristics were systematically investigated for low-cost photosensor/detector applications.

2 Method

2.1 Sample preparation

The chemical bath deposition (CBD) technique [36] was used to prepare ZnO and Mg-doped ZnO thin films on a glass substrate, as shown in Fig. 1. The AR grade quality materials were used as source materials for deposition. These are the source materials for the deposition of pure and Mg-doped ZnO thin films: zinc nitrate hexahydrate, magnesium nitrate hexahydrate and thiourea. The glass substrate was cleaned before deposition using dilute HCl for 3Hr and then acetone and distilled water sequentially in an ultrasonication bath. For the deposition of pure zinc oxide (ZnO) thin film, 0.1 M Zinc nitrate hexahydrate were dissolved in 30 ml DI water and 0.1 M thiourea were dissolved in 30 ml DI water, separately and kept on stirring. Then in metal precursor (Zinc) solution 2 drops of Triethanolamine (TEA) added and stir for 30 min. Then the pH of metal precursor (Zinc) solution maintained at pH 10 by adding ammonia dropwise and then kept on stirring for 15 min. After that thiourea precursor was added to the metal precursor (zinc solution) and kept on stirring at room temperature for 10 min. The dry precleaned glass substrate was immersed vertically in the final solution. The beaker was kept in a water bath and the bath temperature was maintained at 65 °C for 60 min. After 60 min the final reaction was completed and the deposited films were removed. The deposited substrates get washed with the DI water and dried in an air furnace for 1 h subsequently.

Fig. 1

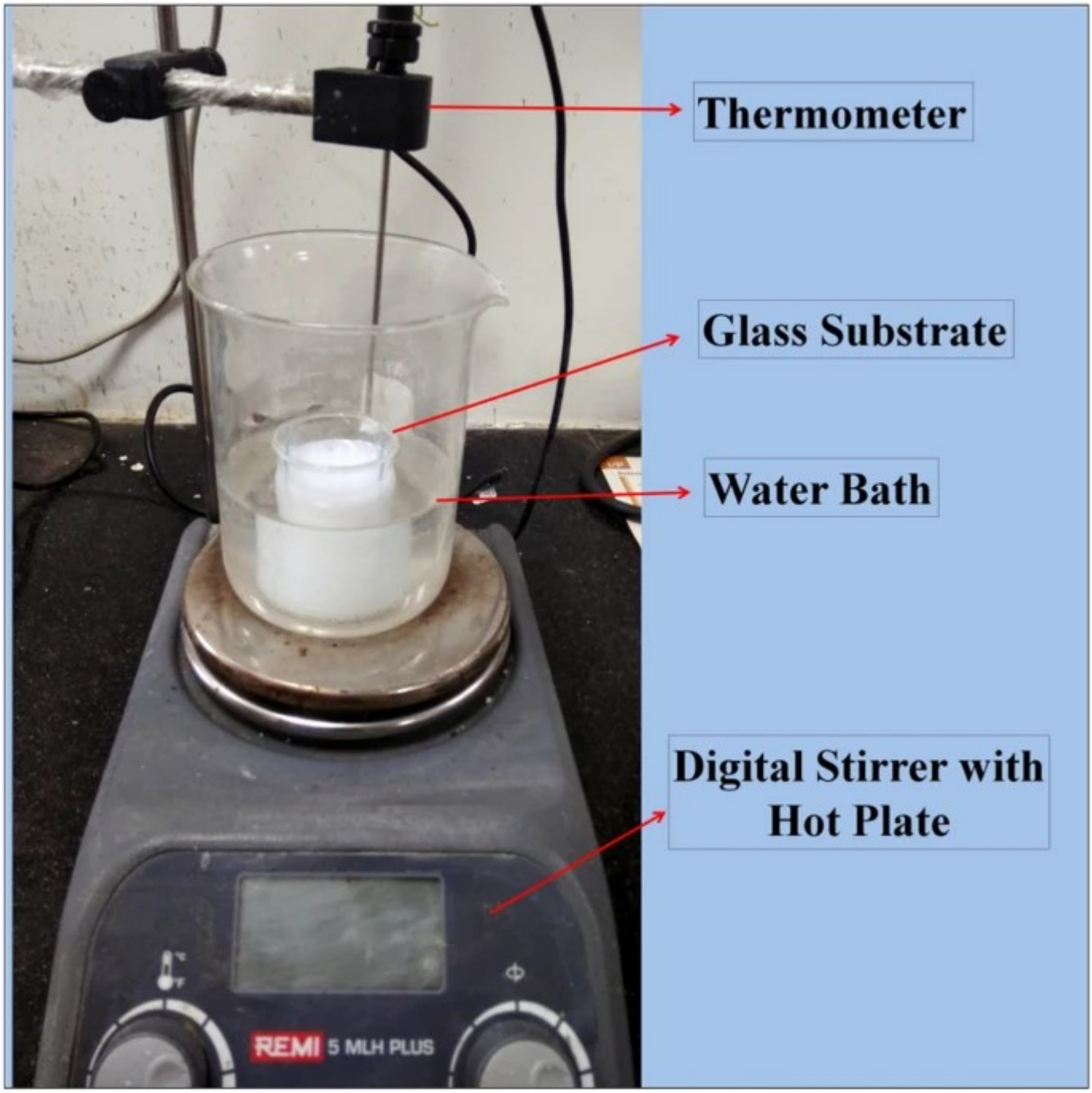

Schematic diagram of chemical bath deposition for pure-ZnO, $Zn_{0.9}Mg_{0.1}O$ and $Zn_{0.8}Mg_{0.2}O$ thin films

The same route was followed for the deposition of Magnesium doped ZnO thin films, in this case [$Mg(NO_3)_2$. $6H_2O$] was added as a Mg source with the concentration 10% and 20% were dissolved separately in 30 ml DI water and then added to the Zn precursor solution.

2.2 Materials characterization

X-ray diffraction (XRD) using D-8 advanced diffractometer (Bruker AXS, Germany) with a monochromatic CuKα radiation source was used to determine crystal structure & structural parameters of the films. In order to get absorption coefficient and bandgap tuning properties the UV–Vis spectrophotometer Perkin Elmer Lambda-25 was used. The Raman spectra of the films were registered by using an Ar ion laser with 514.5 nm wavelength and 50 mW powers as the excitation source. The photoluminescence (PL) properties were studied at room temperature using a He–Cd laser in the spectral range of 300–800 nm with a wavelength of 325 nm as the excitation source. Film morphology was analyzed by field emission scanning electron microscope (FE-SEM): MIRA II LMH from TESCAN, with a resolution of 1.5 nm at 30 kV. KEITHLEY 2400 source meter setup was used to determine the photosensing with the AM 1.5 (300 W/cm^2) solar simulator having monochromatic light source.

3 Results and discussions

3.1 X-ray diffraction analysis

The structural analysis of pure-ZnO, $Zn_{0.9}Mg_{0.1}O$ and $Zn_{0.8}Mg_{0.2}O$ thin films were investigated by using X-ray diffraction patterns as shown in Fig. 2. As compared with JCPDS #36-1451 the all peaks (100), (002), (101), (102), (110), (103), and (112) corresponding to pure-ZnO exhibiting a wurtzite structure ($P6_3mc$) with preferential orientation along the *c*-axis and diffraction pattern indicates polycrystalline nature of the film [27, 37]. For Mg-ZnO thin films in Fig. 2, the intensity of the (002) peak decreases and (100) & (101) peaks intensity increases slightly, with a very low broadening at increasing Mg concentrations. This suggests that the incorporation of Mg in the ZnO structure does not markedly affect the crystallinity of the films due to the less difference in ionic radii of Mg (0.57 Å) atoms and Zn (0.60 Å) atoms.

Fig. 2

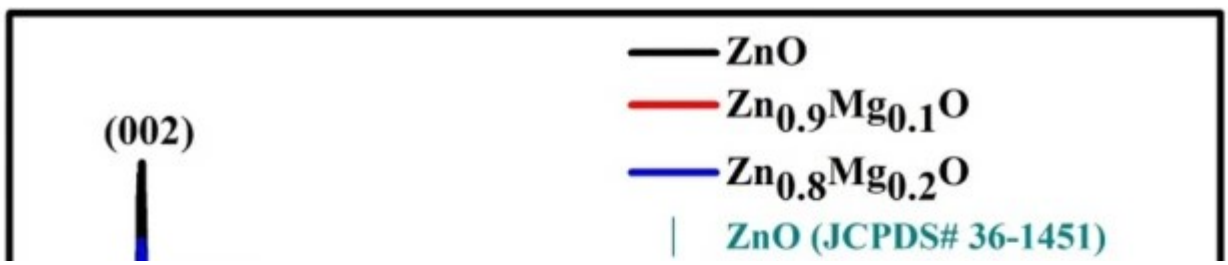

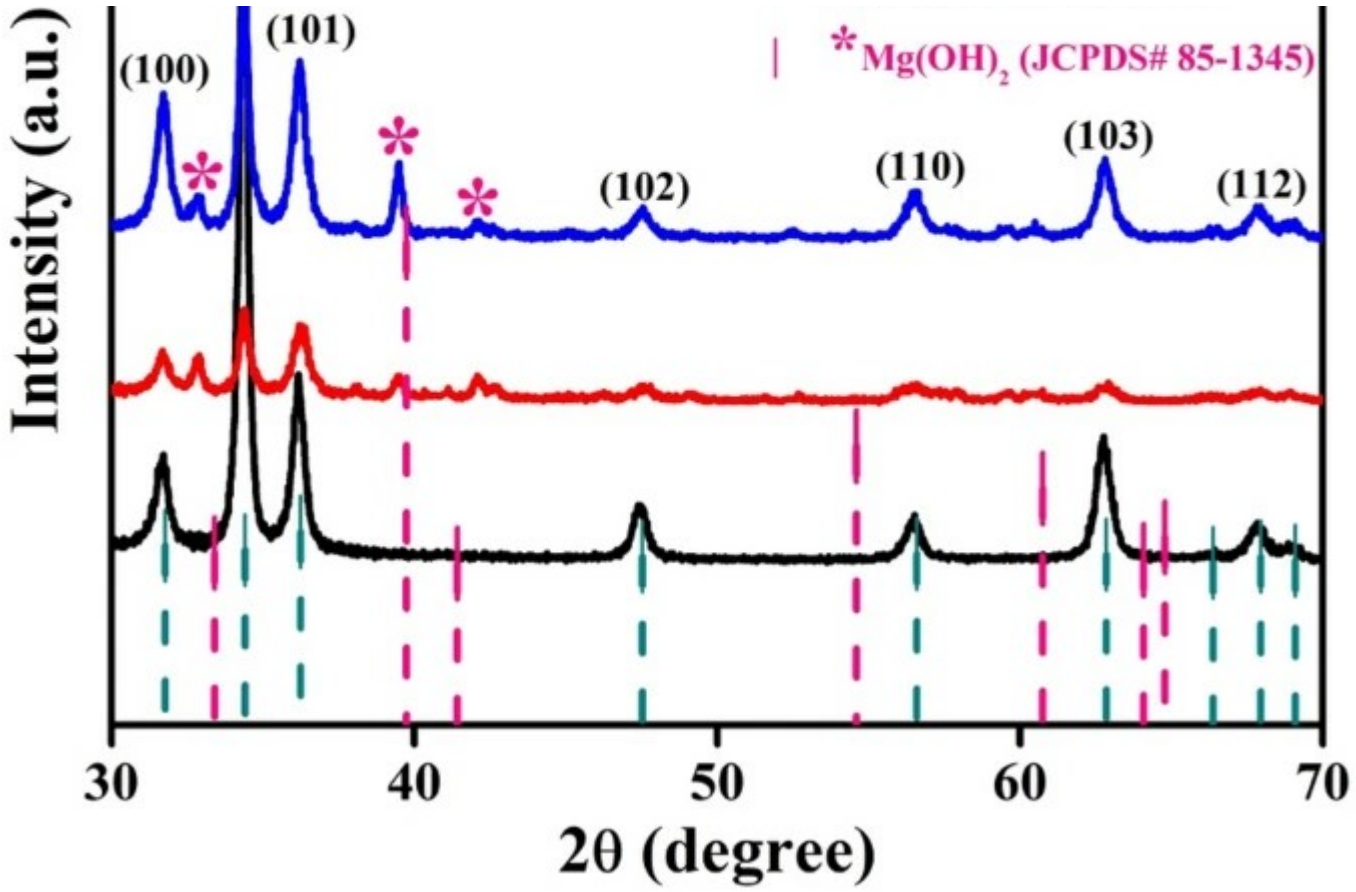

X-ray diffraction patterns of pure-ZnO, $Zn_{0.9}Mg_{0.1}O$ and $Zn_{0.8}Mg_{0.2}O$ thin films

From Fig. 2 the diffraction peaks for $Zn_{0.9}Mg_{0.1}O$ and $Zn_{0.8}Mg_{0.2}O$ thin films the 2θ values at 32.89° (100), 39.55° (011) and 42.48° (002) belonging to Brucite-Magnesium hydroxide *$Mg(OH)_2$ phase compared with standard data JCPDS card #85-1345. For 10% Magnesium in ZnO, we can see that phase segregation has been started and furthermore these peaks intensity increases as the concentration of Mg increases to 20% which was also reported by P. Kumar et al. [38]. Using Debye Scherer's formula, [39] the crystallite size (*D*), lattice constants [40], dislocation density (\(\delta)\) [41] and strain \((\varepsilon)\) evaluated by following Eqs. (1), (2), (3), and (4) respectively.

$$D = \frac{0.94\lambda }{{\beta \cos \theta }}$$

(1)

$$\delta = \frac{1}{{D^{ \wedge } 2}}$$

(2)

$$\frac{1}{{d^{2} }} = \frac{4}{3}\left({\frac{{h^{2} + hk + k^{2} }}{{a^{2} }}} \right) + \frac{{l^{2} }}{{c^{2} }}$$

(3)

$$\left(\varepsilon \right) = \frac{\beta \cos \theta }{4}$$

(4)

Factors like phase segregation and agglomeration which affects after certain Mg dopant content it start distortion in ZnO crystal structure and shows the non-uniform distribution over the film [38, 42]. Due to which there is a small change in lattice parameter a while parameter c is decreases as Mg content increases and correlate with the shift in position and intensity of plane peaks as seen in Fig. 2. Furthermore, from Table 1, the calculated average crystallite size shows some random variations, such as first decreased for Mg-10% and then increases for Mg-20% which was calculated from the FWHM values of all the peaks. However, dislocation density and strain both are inversely proportional to the crystallite size; so the resulting calculated values are opposite to the crystallite size, such as for Mg-10% increases and for Mg-20% decreases.

Table 1 Microstructural parameters of pure-ZnO, $Zn_{0.9}Mg_{0.1}O$ and $Zn_{0.8}Mg_{0.2}O$ thin films

3.2 UV–Vis spectroscopy

Optical properties of pure-ZnO, $Zn_{0.9}Mg_{0.1}O$ and $Zn_{0.8}Mg_{0.2}O$ thin films were elucidated from UV–Vis spectroscopy as depicted in Fig. 3. The observed absorption spectra in the range of 300–900 nm and the absorption peaks detected around at 441, 434 and 341 nm for pure-ZnO, $Zn_{0.9}Mg_{0.1}O$ and $Zn_{0.8}Mg_{0.2}O$ thin films respectively, due to the photoexcitation of electrons from the valence to the conduction band. The Band gap was intended from Tauc's relation,

given in Eq. (5) [43],

$$\alpha hv = A\left({hv - E_{g} } \right)^{{{1 \mathord{\left/ {\vphantom {1 2}} \right. \kern-\nulldelimiterspace} 2}}}$$

(5)

Fig. 3

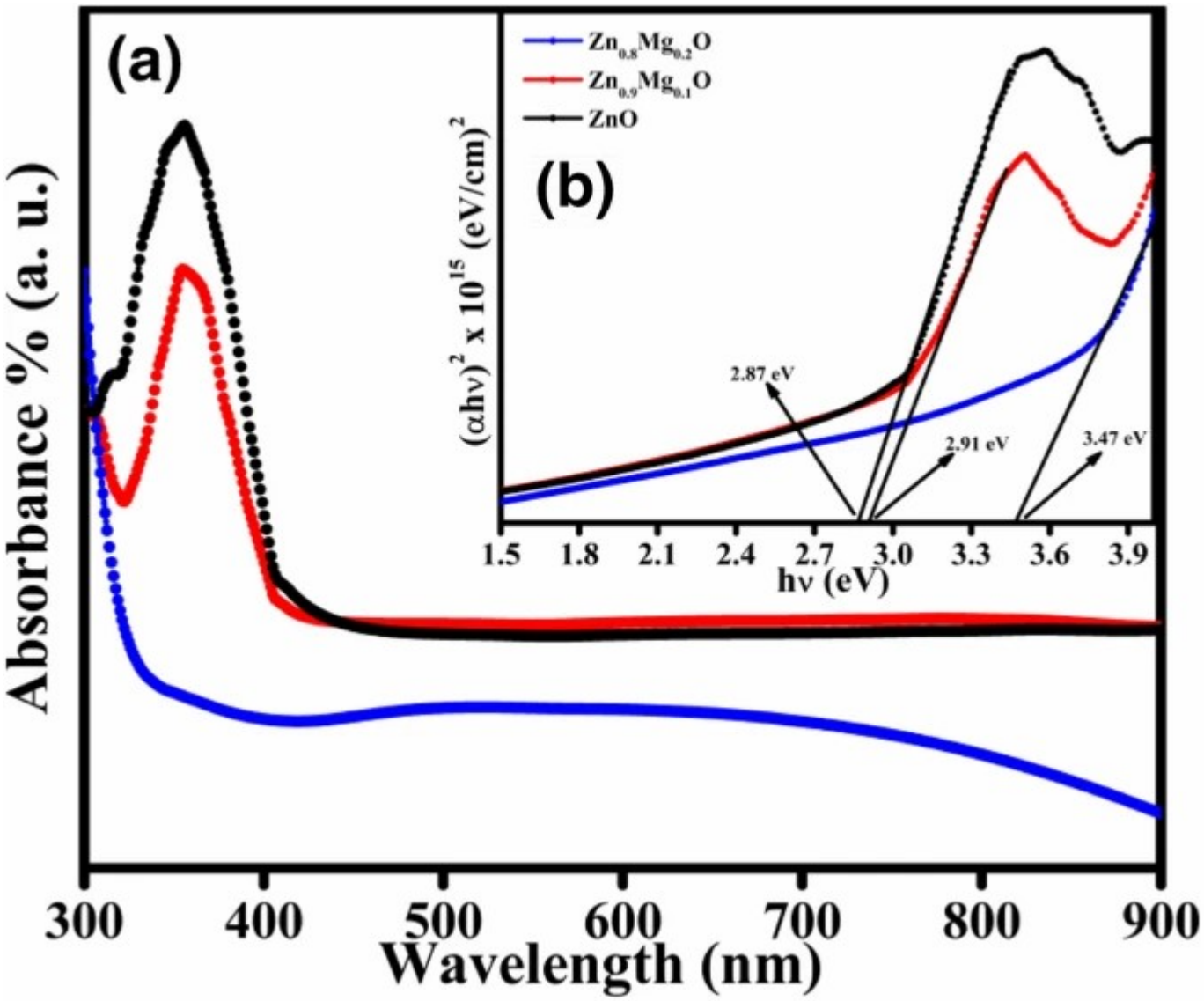

(a) UV absorption spectrum, (b) Tauc's plot of the pure-ZnO, $Zn_{0.9}Mg_{0.1}O$ and $Zn_{0.8}Mg_{0.2}O$ thin films

where α is the absorption coefficient, h is the Planck's constant and v is the frequency of light.

The bandgap obtained from the Tauc's Plot of the pure-ZnO, $Zn_{0.9}Mg_{0.1}O$ and $Zn_{0.8}Mg_{0.2}O$ thin films are 2.96 eV and 3.02 eV & 3.42 eV, respectively [38, 44,45,46,47]. As the concentration of Mg in ZnO increases which enhance the bandgap and this effect ascribed to Moss-Burstein effect. PL studies gives support to the increment in optical band gap energy as Mg concentration increases in ZnO; however resulting in the modifications of electrical properties of Mg-doped ZnO thin films [48]. Furthermore, increased electron concentration and oxygen vacancies due to the variations in electronegativity and the ionic radius of Zn^{2+} and Mg^{2+} [49, 50]. This blue-shift in the band gap is the radiative recombination of the bound excitons that decreases the emission wavelength of the band edge and can be assisted by the change in the size of the crystallite [50]. Because doping concentration of Mg represents from 10 to 20%; the number of bound excitons is also increased and the energy levels situated at the bottom of the conduction band are taken up by these excitons.

3.3 Raman spectroscopy analysis

Raman scattering studies of pure-ZnO, $Zn_{0.9}Mg_{0.1}O$ and $Zn_{0.8}Mg_{0.2}O$ thin films has been carried out and resulting spectra are depicted in Fig. 4. This spectroscopic method used to analyze the detailed information on molecular vibrations chemical structures, and sample crystallinity is non-destructive chemical analysis. There are two modes: acoustic modes and optical modes [51]. Both A1 & E1 modes (infrared active) splits into transverse optical (TO) and longitudinal optical (LO). Two non-polar phonon modes of E2 (high) & E2 (low) reflecting oxygen movement and Zn sublattice movement, respectively. A Raman scattering of the pure-ZnO thin film gives a sharp peak at 437 cm^{-1} assigns to the Raman active E2 (high) mode, which corresponds to the hexagonal wurtzite phase of ZnO [52, 53]. Also, three small peaks at 334 cm^{-1}, 380 cm^{-1} and 580 cm^{-1} were observed [54], and which are assigned to multiple phonon processes. Observed peaks at 334 cm^{-1} and 380 cm^{-1} are A1 (TO) phonon mode and E1 (LO) mode, respectively which are correlated to the distortion in lattice constant values of cations. However, 380 cm^{-1} and 437 cm^{-1} peaks for Mg-doped ZnO thin films has been blue-shifted to 407 cm^{-1*} and 479 cm^{-1*} respectively, as shown in Fig. 4 [51]. The existence of long range electrostatic order was confirmed from the observed peak at 580 cm^{-1} corresponds to E1 (LO) mode in pure-ZnO system. The phase segregation and structural defects which are

confirmed from XRD data in Fig. 2; also responsible for Raman-shift and disappearance of peaks for Mg-doped ZnO thin films [55].

Fig. 4

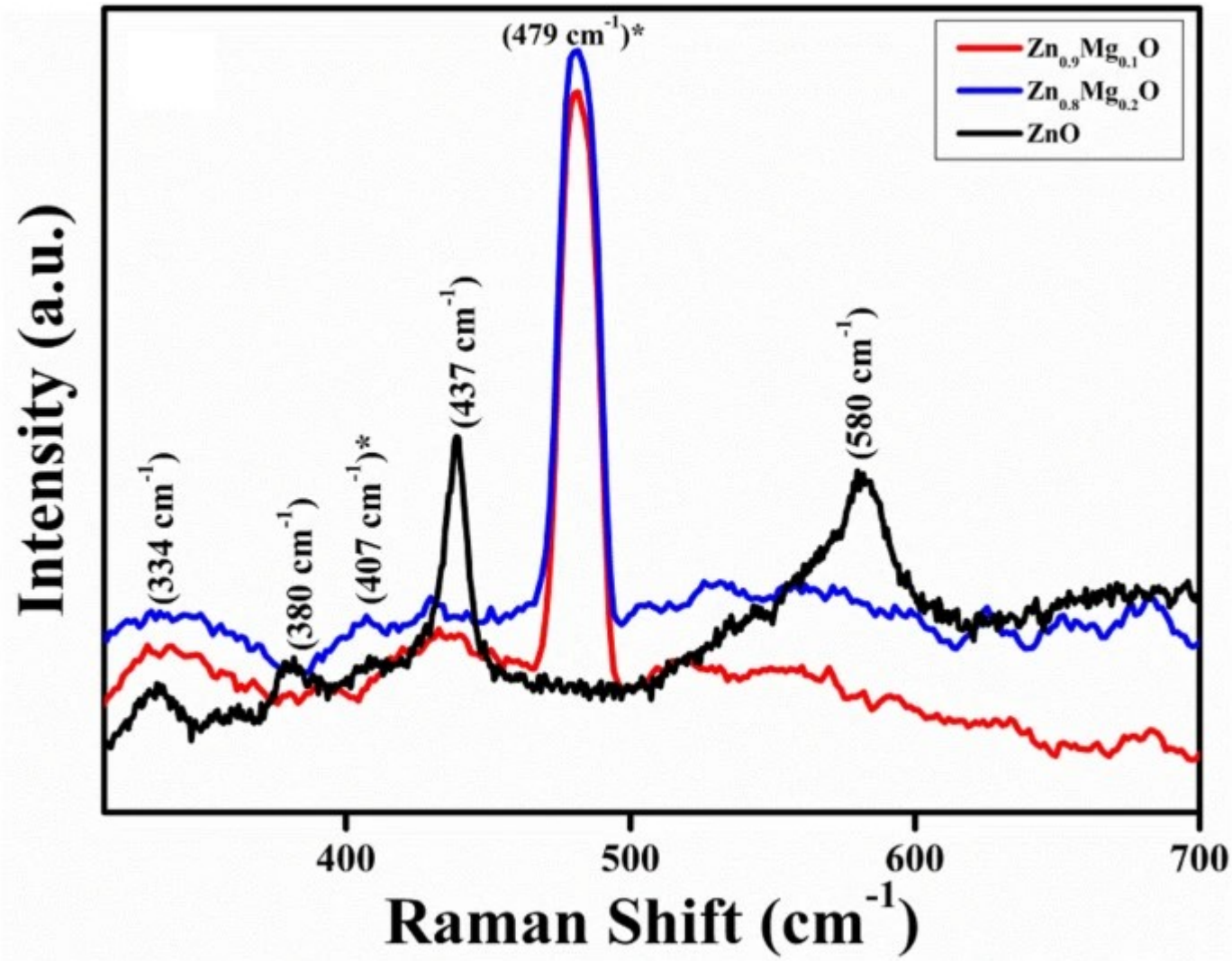

Raman spectra of pure-ZnO, $Zn_{0.9}Mg_{0.1}O$ and $Zn_{0.8}Mg_{0.2}O$ thin films

3.4 Photoluminescence study

Figure 5 shows the normalized photoluminescence spectra of pure-ZnO, $Zn_{0.9}Mg_{0.1}O$ and $Zn_{0.8}Mg_{0.2}O$ thin films which measured at room temperature with an excitation wavelength of 450 nm. PL spectra show three bands of emissions in both pure ZnO and Mg-doped ZnO thin films which centered at 390 nm (3.18 eV) in the UV region, 450 nm (2.75 eV) in the visible

region and 560 nm (2.21 eV). These emission peaks are related to the near-band edge (NBE), and deep-level (DLE) emissions respectively [52, 53]. NBE emissions are attributed to free exciton emissions (typical bandgap transition) whereas DLE is attributed to zinc vacancies in the ZnO lattice [56,57,58,59,60,61]. DLE (Green and green-yellow luminescence) band peaks are attributed due to some self-activated defects center and derive from zinc vacancies in ZnO at the wavelengths of approximately 520 and 560 nm, respectively [56, 62,63,64,65]. Similarly in Mg-doped ZnO nanostructures, the PL emission peaks were found centered at around 380 nm (3.26 eV), 450 nm (2.75 eV), 480 nm (2.58 eV) & 580 nm (2.13 eV). In our study, the Mg-doped ZnO samples show a broad emission band at around 450 nm and 560 nm is assigned to zinc and oxygen vacancies, respectively [66,67,68,69]. This broad emission band intensity is improved after Mg doping concentration due to an increase in vacancy concentration [38, 70, 71]. In addition to this phase segregation due to excess of Mg content in ZnO lattice possibly helps to increase the defects and resulting increases the intensity of PL peaks in DLE region. Mg-doped ZnO hexagonal rods thin films luminescence spectra not only cover the UV emission but also cover-up the visible range which makes this material as a strong candidate for near-white-light-emitting material.

Fig. 5

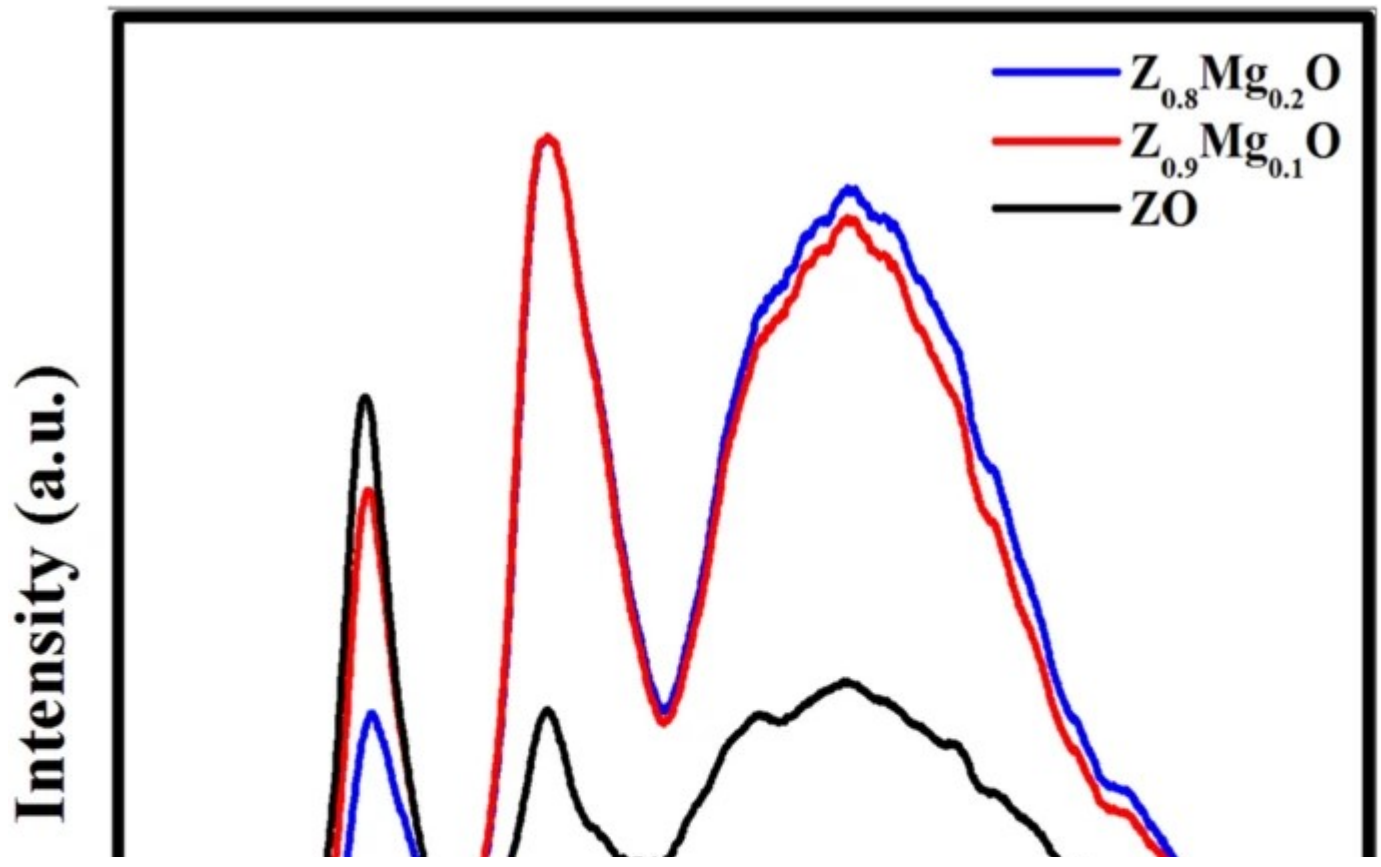

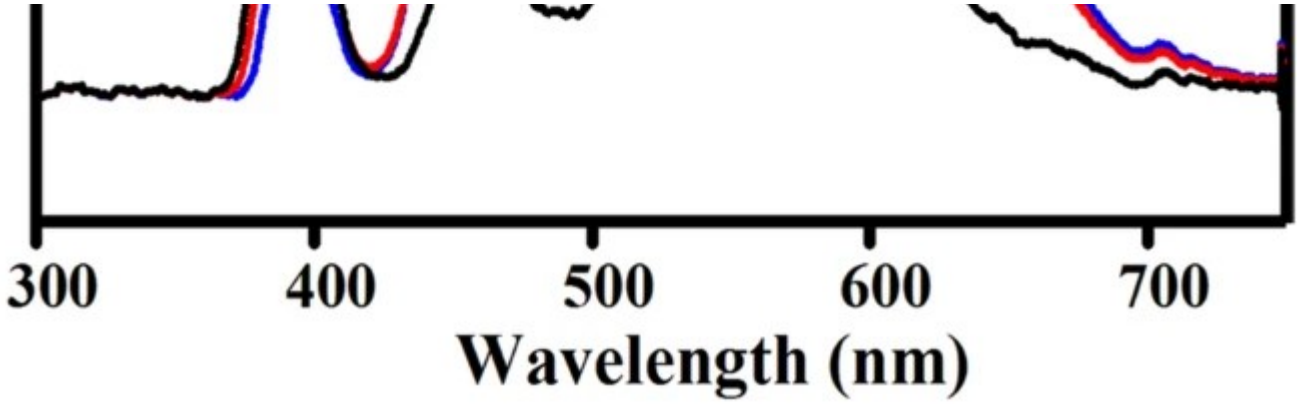

Photoluminescence of pure-ZnO, $Zn_{0.9}Mg_{0.1}O$ and $Zn_{0.8}Mg_{0.2}O$ thin films

3.5 Surface morphological studies

In order to confirm the morphology FE-SEM studies were carried out for synthesized pure-ZnO, $Zn_{0.9}Mg_{0.1}O$ and $Zn_{0.8}Mg_{0.2}O$ thin films. In the Fig. 6 we can clearly see that the agglomerates of hexagonal rod like structures are formed in pure ZnO thin films while conical rods can be seen in Mg-doped ZnO thin films. It is observed from Fig. 6 micrographs for ZnO hexagonal rods are well cover the substrate and we can see clearly the growth of rods along the plane *c*-axis (002), which confirms with the XRD pattern. For Mg doped ZnO thin films, the hexagonal rods of ZnO are distorted as seen in Fig. 6b and c. Hexagonal rods are become cone-like structure for Mg-doped ZnO thin films, due to the growth along (101) plane than the (002) plane as evident from XRD results [72]. With increasing Mg content, owning to nuclei aggregation and the Ostwald ripening process, these rods get more stacked together and form a flower-like structure [73]. Also, Sankar R. et al. (2017) has observed the morphological changes, hexagonal nanorods into irregular sphere-like morphology (nanoparticles) after excessive doping of aluminium (Al) in ZnO [74] and Bharathi et al. (2019) observed the agglomeration in ZnO nanorods morphology with Gadolinium (Gd) dopant, such as increasing the concentration of Gd in ZnO the hexagonal nanorods are tends to flower-like structure [75].

Fig. 6

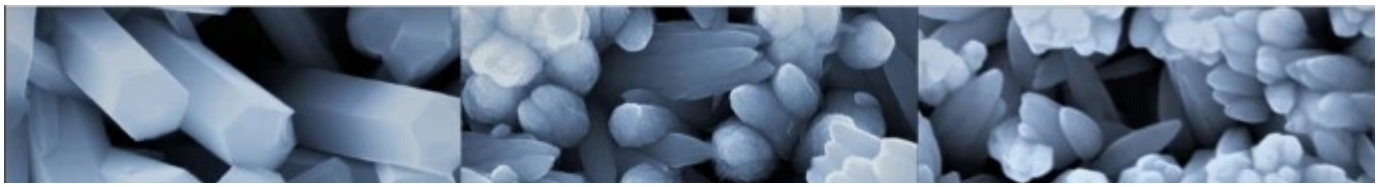

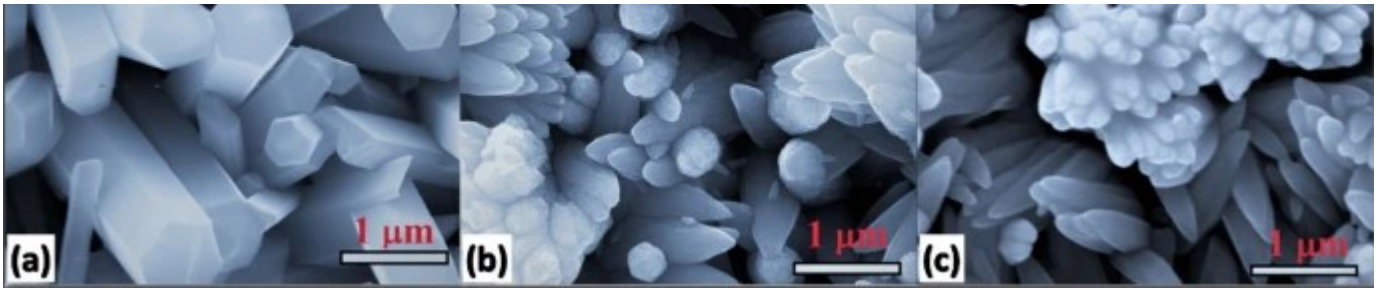

surface morphological image of (a) pure-ZnO, (b) $Zn_{0.9}Mg_{0.1}O$ and (c) $Zn_{0.8}Mg_{0.2}O$ thin films

3.6 *I–V* characteristics study

Current (*I*) vs voltage (*V*) characteristics studied for pure-ZnO, $Zn_{0.9}Mg_{0.1}O$ and $Zn_{0.8}Mg_{0.2}O$ hexagonal rods thin films under dark and illumination of light condition [34]. Figure 7a–c displays the *J–V* plot of pure-ZnO, $Zn_{0.9}Mg_{0.1}O$ and $Zn_{0.8}Mg_{0.2}O$ thin films photosensing in dark and under the illumination of light. In the *J–V* plot, current density (*J*) was calculated from the observed current (*I*) values divided by area (A) of the deposited film. The adsorption and desorption of oxygen molecules plays a crucial role in photoconduction in the photoresponse mechanism of ZnO photosensors. In the dark condition, oxygen molecules adsorbed from an ambient atmosphere on the ZnO layer surface according to the equation; \({\mathrm{O}}_{2} \left(gas\right)+ {\mathrm{e}}^{-} \left(surface\right)\to {\mathrm{O}}_{2}^{-} (adsorption)\) and form a region of low conductivity depletion. Electron–hole ($e^- - h^+$) pairs are photogenerated underexposure to light illumination, where oxygen molecules desorb from the ZnO surface due to photogenerated holes which indorsed to decrease the depletion width of low conductivity as follows, \({h}^{+}+ {O}_{2}^{-} \left(adsorption\right)\to {O}_{2 }(gas)\) [76].

Fig. 7

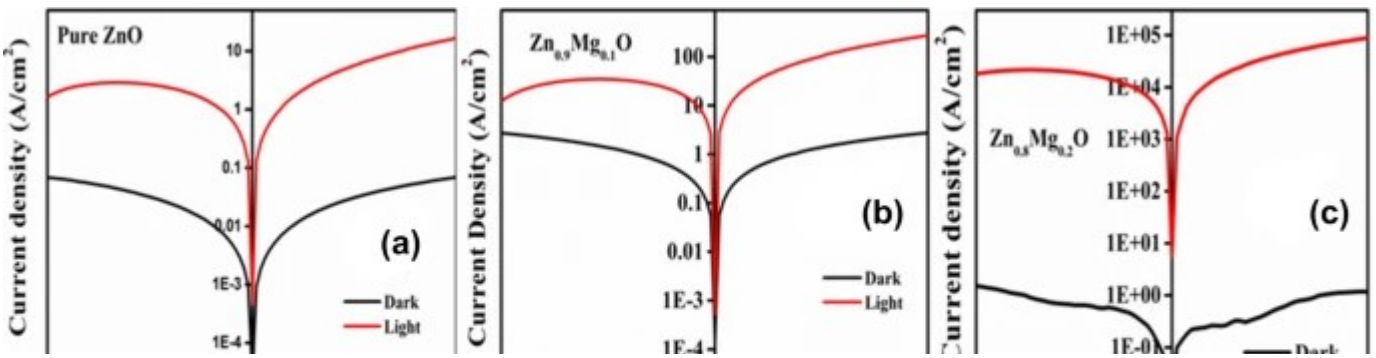

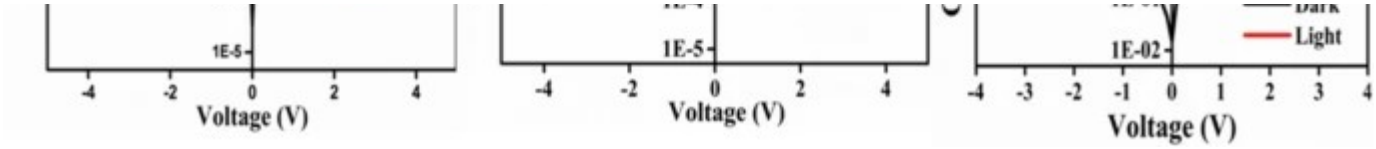

J–*V* characteristics of (a) pure-ZnO, (b) $Zn_{0.9}Mg_{0.1}O$, and (c) $Zn_{0.8}Mg_{0.2}O$ thin films

Furthermore, in Mg-doped ZnO thin films, due to less difference in ionic radius and electronegativity between Mg^{2+} and Zn^{2+} they may alloy significantly by replacing each other without affecting the lattice constant of ZnO structure [72]. Large amounts of generated point defects have detrimental effects on the optical properties which enhance the performance of ZnMgO devices [58, 77]. Even, on the surface, the as-grown ZnMgO layer includes hydroxyl bonds, which break by photon exposure. As a donor atom, the H atoms from the broken hydroxyl bonds shift to the ZnMgO lattice interstitial site. The resistivity of the ZnMgO layer reduces with the generation of H atoms, consequently the efficiency increases. In addition, the specific benefits of the ZnMgO alloy as a photosensor are the large optical absorption and high photosensitivity in the visible region [34]. From the *J*–*V* curve, we can say that as the percentage of doping increases in Mg-doped ZnO thin films, photosensitivity is improved. As confirmed from XRD spectra, this can be attributed to the MgO phase. Also, from PL spectra the deep level defects are due to zinc and oxygen vacancies are generated in the doped film. The Fig. 7 results clearly show that the abrupt increment in J_{SC} values under monochromatic light source. Resistance and photocurrent of the pure-ZnO, $Zn_{0.9}Mg_{0.1}O$ and $Zn_{0.8}Mg_{0.2}O$ thin films in dark and under illumination is tabulated below in Table 2 and the values are tabulated in Table 2 are considered as an ideal for photosensors according to literature [78, 79]. Also, the presence of a high density of hole-trap states on the surface of the nanorods significantly affects the characteristics of transport and photoconduction due to the high surface-to-volume ratio. Under dark, due to the adsorption of oxygen molecules on the oxide surface that absorbs the free electrons present in the *n*-type oxide semiconductor, a low-conductivity depletion layer is formed near the surface [34]. Under the monochromatic light source absorbing the photon energy and produced electron–hole pairs; holes migrate to the surface and discharge the adsorbed oxygen ions negatively charged, which allows desorption of oxygen [80]. The unpaired electrons are either captured at the anode or recombined with holes formed by adsorption and ionization of oxygen molecules on the surface. Because of the

surface-to-surface bonds and zinc vacancies which attributed the high density trap states and that improves the photoresponse of nanorods. The Eq. (6) determined the photosensitivity of the pure-ZnO, $Zn_{0.9}Mg_{0.1}O$ and $Zn_{0.8}Mg_{0.2}O$ thin films under monochromatic light source AM 1.5 solar simulator [81],

$$S\left(\% \right) = \frac{{R_{d} - R_{I} }}{{R_{d} }} \times 100$$

(6)

Table 2 The calculated current & resistance of the pure-ZnO and $Zn_{0.9}Mg_{0.1}O$ and $Zn_{0.8}Mg_{0.2}O$ thin films in dark and under illumination were tabulated below

where R_d and R_l are the resistances under dark and light condition respectively. Furthermore, photoresponse was evaluated from photocurrent rise and decay w. r. to time by switching (on and off) continously the monochromatic light source with different illumination power (range 100 W to 300 W) at an applied bias voltage of 2 V. The results are depicted in Fig. 8a. In addition to this the response and recovery time was calculated for pure-ZnO, $Zn_{0.9}Mg_{0.1}O$ and $Zn_{0.8}Mg_{0.2}O$ thin films for 100 W illumination as shown in Fig. 8b. However the charge carrier traps and defects states are responsible for high recovery time and less response time. The response, recovery and photosensing parameters results are compared with the previously reported 1D photosensors and tabulated below in Table 3. The results of the Mg-doped ZnO hexagonal rods thin films shows the effective photosensing performance as visible photosensor.

Fig. 8

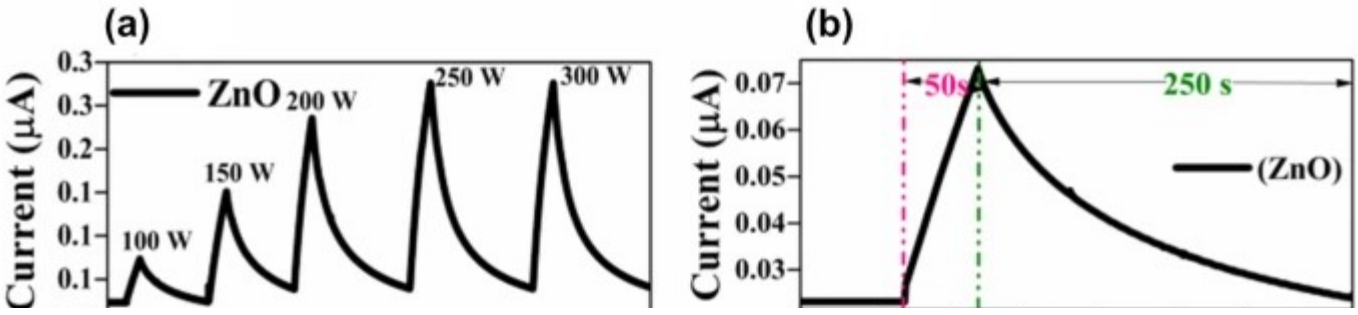

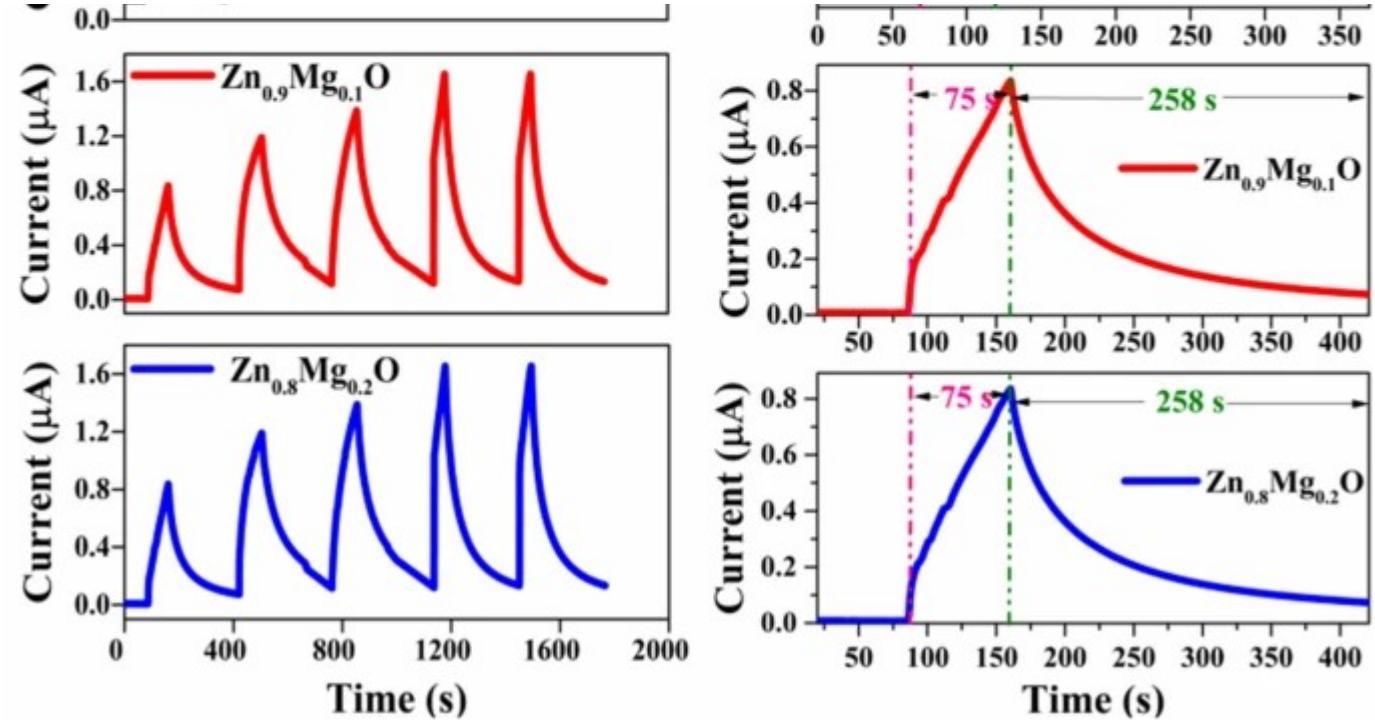

Photo-response of pure-ZnO, $Zn_{0.9}Mg_{0.1}O$, and $Zn_{0.8}Mg_{0.2}O$ 1-D hexagonal rods thin film for (a) varying power from 100 to 300 W/ cm^2 and for (b) 100 W/cm^2 power

Table 3 Response, recovery time, photosensitivity vs. power of pure-ZnO and $Zn_{0.9}Mg_{0.1}O$ and $Zn_{0.8}Mg_{0.2}O$ 1D hexagonal rods thin films

4 Conclusion

In this compendium, the highly photosensitive Mg-doped ZnO hexagonal rods thin films are well prepared using cost-effective and simple chemical bath deposition method. The synthesized pure-ZnO and $Zn_{0.9}Mg_{0.1}O$ and $Zn_{0.8}Mg_{0.2}O$ thin films were characterized for their structural, morphological, optical and electrical properties. The structural and morphological properties were analyzed via XRD and SEM characterization techniques; confirmed the formation of hexagonal rod-like structure for pure-ZnO and for Mg-doped ZnO samples there were found some structural changes like hexagonal rods become conical rods. As we increase the Mg content 10 to 20% in ZnO structure, phase segregation process gets

started and also due to agglomeration the conical rods are stacked with each other in large amount shows flower-like structure in $Zn_{0.8}Mg_{0.2}O$ sample. It can be clearly seen in SEM images. The effect of electron–phonon interaction from Raman analysis also confirmed the phase segregation due to the large shift in E2 (high) mode. The optical properties showed an increase in optical bandgap with Mg doping and PL study confirmed the increase in surface defects as well as deep-level defects generated within the visible range which was also increases as Mg content increases. However, these overall results with the Mg doping helps to enhance the photosensing properties in terms of measured less resistivity, high photocurrent and *J*–*V* result showed a significant enhancement in photosensitivity of Mg-doped ZnO hexagonal rods thin films.

References

1. S.R. Tamalampudi, Y.-Y. Lu, R.U. Kumar et al., Nano Lett. 14, 2800 (2014). https://doi.org/10.1021/nl500817g

Article CAS Google Scholar

2. Y. Ye, L. Dai, X. Wen, P. Wu, R. Pen, G. Qin, ACS Appl. Mater. Interfaces 2, 2724 (2010). https://doi.org/10.1021/am100661x

Article CAS Google Scholar

3. D.C. Oertel, M.G. Bawendi, A.C. Arango, V. Bulović, Appl. Phys. Lett. 87, 213505 (2005). https://doi.org/10.1063/1.2136227

Article CAS Google Scholar

4. O. Lopez-Sanchez, D. Lembke, M. Kayci, A. Radenovic, A. Kis, Nat. Nanotechnol. 8, 497 (2013). https://doi.org/10.1038/nnano.2013.100

Article CAS Google Scholar

5. H. Liu, N. Gao, M. Liao, X. Fang, Sci. Rep. 5, 7716 (2015). https://doi.org/10.1038/srep07716

Article CAS Google Scholar

6. L. Li, E. Auer, M. Liao et al., Nanoscale 3, 1120 (2011). https://doi.org/10.1039/C0NR00702A

Article CAS Google Scholar

7. L.X. Qian, X.Z. Liu, T. Sheng, W.L. Zhang, Y.R. Li, P.T. Lai, AIP Adv. 6, 045009 (2016). https://doi.org/10.1063/1.4947137

Article CAS Google Scholar

8. C.-H. Liao, C.-W. Huang, J.-Y. Chen et al., J. Phys. Chem. C 118, 8194 (2014). https://doi.org/10.1021/jp500830x

Article CAS Google Scholar

9. C. Zhang, Y. Xie, H. Deng et al., Small 13, 1604197 (2017). https://doi.org/10.1002/smll.201604197

Article CAS Google Scholar

10. U.M. Nayef, K.A. Hubeatir, Z.J. Abdulkareem, Optik 127, 2806 (2016). https://doi.org/10.1016/j.ijleo.2015.12.002

Article CAS Google Scholar

11. S.P. Ghosh, K.C. Das, N. Tripathy et al., IOP Conf. Ser.: Mater. Sci. Eng. 115, 012035 (2016). https://doi.org/10.1088/1757-899x/115/1/012035

Article CAS Google Scholar

12. K. Liu, M. Sakurai, M. Aono, Sensors (Basel) 10, 8604 (2010). https://doi.org/10.3390/s100908604

Article CAS Google Scholar

13. C.G. Núñez, A. Vilouras, W.T. Navaraj, F. Liu, R. Dahiya, IEEE Sens. J. 18, 7881 (2018). https://doi.org/10.1109/JSEN.2018.2853762

Article Google Scholar

14. C. Soci, A. Zhang, B. Xiang et al., Nano Lett. 7, 1003 (2007). https://doi.org/10.1021/nl070111x

Article CAS Google Scholar

15. J. Mallows, M. Planells, V. Thakare, R. Bhosale, S. Ogale, N. Robertson, ACS Appl. Mater. Interfaces 7, 27597 (2015). https://doi.org/10.1021/acsami.5b09291

Article CAS Google Scholar

16. Z. Ji, X. Wang, H. Zhang et al., ACS Nano 6, 5366 (2012). https://doi.org/10.1021/nn3012114

Article CAS Google Scholar

17. N.M. Abd-Alghafour, N.M. Ahmed, Z. Hassan, Sens. Actuators A 250, 250 (2016). https://doi.org/10.1016/j.sna.2016.09.001

Article CAS Google Scholar

18. Y. Huang, J. Lin, L. Li et al., J. Mater. Chem. C 3, 5253 (2015). https://doi.org/10.1039/C5TC00453E

Article CAS Google Scholar

19. H. Liu, Z. Zhang, H. Linfeng et al., Adv. Opt. Mater. (2014). https://doi.org/10.1002/adom.201400176

Article Google Scholar

20. D.-H. Lien, J.R. Durán Retamal, J.-J. Ke, C.-F. Kang, J.-H. He, Nanoscale 7, 19874 (2015). https://doi.org/10.1039/C5NR06494E

Article CAS Google Scholar

21. C.O. Chey, A. Masood, A. Riazanova et al., J Nanomater 2014, 9 (2014). https://doi.org/10.1155/2014/524530

Article CAS Google Scholar

22. N. Kouklin, Adv. Mater. 20, 2190 (2008). https://doi.org/10.1002/adma.200701071

Article CAS Google Scholar

23. S.V. Mohite, K.Y. Rajpure, Opt. Mater. 36, 833 (2014). https://doi.org/10.1016/j.optmat.2013.12.007

Article CAS Google Scholar

24. C.-Y. Hsu, D.-H. Lien, S.-Y. Lu et al., ACS Nano 6, 6687 (2012). https://doi.org/10.1021/nn3011625

Article CAS Google Scholar

25. R. Khokhra, B. Bharti, H.-N. Lee, R. Kumar, Sci. Rep. 7, 15032 (2017). https://doi.org/10.1038/s41598-017-15125-x

Article CAS Google Scholar

26. Y. Li, F.D. Valle, M. Simonnet, I. Yamada, J.-J. Delaunay, Appl. Phys. Lett. 94, 023110 (2009). https://doi.org/10.1063/1.3073042

Article CAS Google Scholar

27. L. Guo, Y.L. Ji, H. Xu, P. Simon, Z. Wu, J. Am. Chem. Soc. 124, 14864 (2002). https://doi.org/10.1021/ja027947g

Article CAS Google Scholar

28. C.S. Lao, M.-C. Park, Q. Kuang et al., J. Am. Chem. Soc. 129, 12096 (2007). https://doi.org/10.1021/ja075249w

Article CAS Google Scholar

29. C.-L. Hsu, S.-J. Chang, Small 10, 4562 (2014). https://doi.org/10.1002/smll.201401580

Article CAS Google Scholar

30. D.S. Boyle, K. Govender, P. Orien, Chem. Commun. (2002). https://doi.org/10.1039/B110079N

Article Google Scholar

31. F. Tian, D. Duan, D. Li et al., Sci. Rep. 4, 5759 (2014). https://doi.org/10.1038/srep05759

Article CAS Google Scholar

32. X. Sha, F. Tian, D. Li et al., Sci. Rep. 5, 11003 (2015). https://doi.org/10.1038/srep11003

Article CAS Google Scholar

33. J. Liriano, P. Misra, S. Sahoo, R.S. Katiyar, ECS Trans. 61, 387 (2014). https://doi.org/10.1149/06104.0387ecst

Article CAS Google Scholar

34. A.S. Dive, N.P. Huse, K.P. Gattu, R. Sharma, Sens. Actuators A 266, 36 (2017). https://doi.org/10.1016/j.sna.2017.09.009

Article CAS Google Scholar

35. M. Patil, D. Sharma, A. Dive, S. Mahajan, R. Sharma, Procedia Manuf. 20, 505 (2018). https://doi.org/10.1016/j.promfg.2018.02.075

Article Google Scholar

36. P. More, S. Dhanayat, K. Gattu, S. Mahajan, D. Upadhye, R. Sharma, AIP Conf. Proc. 1728, 020489 (2016). https://doi.org/10.1063/1.4946540

Article Google Scholar

37. V. Mohammad, A. Umar, Y.-B. Hahn, *ZnO Nanoparticles: Growth, Properties, and Applications* (American Scientific Publishers, Valencia, 2010).

Google Scholar

38. P. Kumar, J.P. Singh, Y. Kumar, A. Gaur, H.K. Malik, K. Asokan, Curr. Appl. Phys. 12, 1166 (2012). https://doi.org/10.1016/j.cap.2012.02.042

Article Google Scholar

39. A.L. Patterson, Phys. Rev. 56, 978 (1939). https://doi.org/10.1103/PhysRev.56.978

Article CAS Google Scholar

40. B.E. Warren, *X-Ray Diffraction* (Dover Publications, Mineola, 1990).

Google Scholar

41. E. Muchuweni, T.S. Sathiaraj, H. Nyakotyo, Heliyon 3, e00285 (2017). https://doi.org/10.1016/j.heliyon.2017.e00285

Article CAS Google Scholar

42. P. Kumar, V. Singh, V. Sharma, G. Rana, H.K. Malik, K. Asokan, Ceram. Int. 41, 6734 (2015). https://doi.org/10.1016/j.ceramint.2015.01.117

Article CAS Google Scholar

43. J. Tauc, R. Grigorovici, A. Vancu, Phys. Status Solidi b 15, 627 (1966). https://doi.org/10.1002/pssb.19660150224

Article CAS Google Scholar

44. E. Vinoth, S. Gowrishankar, N. Gopalakrishnan, Appl. Phys. A Mater. (2018). https://doi.org/10.1007/S00339-018-1852-6

Article Google Scholar

45. R. Yousefi, J. Beheshtian, S.M. Seyed-Talebi, H.R. Azimi, F. Jamali-Sheini, Chem-Asian J. 13, 194 (2018). https://doi.org/10.1002/asia.201701423

Article CAS Google Scholar

46. B.K. Sonawane, M.P. Bhole, D.S. Patil, Opt. Quant. Electron. 41, 17 (2009). https://doi.org/10.1007/s11082-009-9317-y

Article CAS Google Scholar

47. M.M. Yan, Y. Li, Y.T. Zhou et al., IEEE Photon. J. (2017). https://doi.org/10.1109/Jphot.2017.2666423

Article Google Scholar

48. A.S. Asvarov, S.S. Makhmudov, A.K. Abduev, A.K. Akhmedov, M.A. Aliev, B.A. Bilalov, J. Nano Electron. Phys. (2016). https://doi.org/10.21272/Jnep.8(4(2)).04053

Article Google Scholar

49. N. Winkler, S. Edinger, W. Kautek, T. Dimopoulos, J. Mater. Sci. 53, 5159 (2018). https://doi.org/10.1007/s10853-017-1959-8

Article CAS Google Scholar

50. S. Choopun, R.D. Vispute, W. Yang, R.P. Sharma, T. Venkatesan, H. Shen, Appl. Phys. Lett. 80, 1529 (2002). https://doi.org/10.1063/1.1456266

Article CAS Google Scholar

51. C. Bundesmann, N. Ashkenov, M. Schubert et al., Appl. Phys. Lett. 83, 1974 (2003). https://doi.org/10.1063/1.1609251

Article CAS Google Scholar

52. R. Zhang, P.-G. Yin, N. Wang, L. Guo, Solid State Sci. 11, 865 (2009). https://doi.org/10.1016/j.solidstatesciences.2008.10.016

Article CAS Google Scholar

53. B. Chen, H.T. Ng, C. Chen, J. Exp. Nanosci. 2, 57 (2007). https://doi.org/10.1080/17458080601013512

Article CAS Google Scholar

54. S. Sitthichai, A. Phuruangrat, T. Thongtem, S. Thongtem, J. Ceram. Soc. Jpn. 125, 122 (2017). https://doi.org/10.2109/jcersj2.16202

Article CAS Google Scholar

55. M. Ghosh, N. Dilawar, A. Bandyopadhyay, A.K. Raychaudhuri, J. Appl. Phys. 106, 084306 (2009)

Article Google Scholar

56. A. van Dijken, E.A. Meulenkamp, D. Vanmaekelbergh, A. Meijerink, J. Lumin. 87–89, 454 (2000). https://doi.org/10.1016/S0022-2313(99)00482-2

Article Google Scholar

57. A. Kumar, S. Thota, S. Varma, J. Kumar, J. Lumin. 131, 640 (2011). https://doi.org/10.1016/j.jlumin.2010.11.008

Article CAS Google Scholar

58. M. Trunk, V. Venkatachalapathy, A. Galeckas, A.Y. Kuznetsov, Appl. Phys. Lett. (2010). https://doi.org/10.1063/1.3518480

Article Google Scholar

59. M. Egblewogbe, B. Anand, R. Podila, R. Philip, S. Sai, A. Rao, Mater. Express 2, 351 (2012). https://doi.org/10.1166/mex.2012.1089

Article CAS Google Scholar

60. D.A. Lucca, D.W. Hamby, M.J. Klopfstein, G. Cantwell, Phys. Status Solidi B 229, 845 (2002)

Article CAS Google Scholar

61. N.C.S. Selvam, R.T. Kumar, L.J. Kennedy, J.J. Vijaya, J. Alloys Compd. 509, 9809 (2011). https://doi.org/10.1016/j.jallcom.2011.08.032

Article CAS Google Scholar

62. X.T. Zhang, Y.C. Liu, J.Y. Zhang et al., J. Cryst. Growth 254, 80 (2003). https://doi.org/10.1016/S0022-0248(03)01143-6

Article CAS Google Scholar

63. K. Vanheusden, W.L. Warren, C.H. Seager, D.R. Tallant, J.A. Voigt, B.E. Gnade, J. Appl. Phys. 79, 7983 (1996). https://doi.org/10.1063/1.362349

Article CAS Google Scholar

64. B. Lin, Z. Fu, Y. Jia, Appl. Phys. Lett. 79, 943 (2001). https://doi.org/10.1063/1.1394173

Article CAS Google Scholar

65. A. Janotti, C.G.V.D. Walle, Appl. Phys. Lett. 87, 122102 (2005). https://doi.org/10.1063/1.2053360

Article CAS Google Scholar

66. D. Fang, C. Li, N. Wang, P. Li, P. Yao, Cryst. Res. Technol. 48, 265 (2013). https://doi.org/10.1002/crat.201200437

Article CAS Google Scholar

67. A.K. Das, A. Srinivasan, J. Mater. Sci. Mater. Electron. 28, 6488 (2017). https://doi.org/10.1007/s10854-017-6336-5

Article CAS Google Scholar

68. C. Abed, C. Bouzidi, H. Elhouichet, B. Gelloz, M. Ferid, Appl. Surf. Sci. 349, 855 (2015). https://doi.org/10.1016/j.apsusc.2015.05.078

Article CAS Google Scholar

69. W. Yu, X. Li, X. Gao, Cryst. Growth Des. 5, 151 (2005). https://doi.org/10.1021/cg049973r

Article CAS Google Scholar

70. H. Gupta, J. Singh, R.N. Dutt et al., Phys. Chem. Chem. Phys. 21, 15019 (2019). https://doi.org/10.1039/C9CP02148E

Article CAS Google Scholar

71. L.N. Dong, Y.X. Wang, J.C. Sun et al., Spectrosc. Spect. Anal. 33, 2051 (2013). https://doi.org/10.3964/j.issn.1000-0593(2013)08-2051-04

Article CAS Google Scholar

72. T.H. Fang, S.H. Kang, J. Alloys Compd. 492, 536 (2010). https://doi.org/10.1016/j.jallcom.2009.11.168

Article CAS Google Scholar

73. D.V. Dake, N.D. Raskar, V.A. Mane et al., Appl. Phys. A 126, 640 (2020). https://doi.org/10.1007/s00339-020-03669-1

Article CAS Google Scholar

74. R. Sankar Ganesh, M. Navaneethan, G.K. Mani et al., J. Alloys Compd. 698, 555 (2017). https://doi.org/10.1016/j.jallcom.2016.12.187

Article CAS Google Scholar

75. P. Bharathi, M. Krishna Mohan, V. Shalini et al., Appl. Surf. Sci. 499, 143857 (2020). https://doi.org/10.1016/j.apsusc.2019.143857

Article CAS Google Scholar

76. B. Dekaoruah, Nanoscale Adv. 1, 2059 (2019). https://doi.org/10.1039/C9NA00130A

Article Google Scholar

77. S. Fujihara, Y. Ogawa, A. Kasai, Chem. Mater. 16, 2965 (2004). https://doi.org/10.1021/cm049599i

Article CAS Google Scholar

78. P. Giri, P. Chakrabarti, Superlatt. Microst. 93, 248 (2016). https://doi.org/10.1016/j.spmi.2016.03.024

Article CAS Google Scholar

79. K. Huang, Z. Tang, L. Zhang et al., Appl. Surf. Sci. 258, 3710 (2012). https://doi.org/10.1016/j.apsusc.2011.12.011

Article CAS Google Scholar

80. A. Kaushal, D. Pathak, R.K. Bedi, D. Kaur, Thin Solid Films 518, 1394 (2009). https://doi.org/10.1016/j.tsf.2009.09.020

Article CAS Google Scholar

81. M. Chandramohan, S. Velumani, T. Venkatachalam, Mater. Sci. Eng. B 174, 205 (2010). https://doi.org/10.1016/j.mseb.2010.03.041

Article CAS Google Scholar

82. C.-C. Lin, W.-H. Lin, Y.-Y. Li, J. Nanosci. Nanotechnol. 9, 2813 (2009). https://doi.org/10.1166/jnn.2009.008

Article CAS Google Scholar

83. X. Xue, T. Guo, Z. Lin, T. Wang, Mater. Lett. 62, 1356 (2008). https://doi.org/10.1016/j.matlet.2007.08.053

Article CAS Google Scholar

84. W. Tian, T. Zhai, C. Zhang et al., Adv. Mater. 25, 4625 (2013). https://doi.org/10.1002/adma.201301828

Article CAS Google Scholar

85. S.-E. Ahn, H.J. Ji, K. Kim et al., Appl. Phys. Lett. 90, 153106 (2007). https://doi.org/10.1063/1.2721289

Article CAS Google Scholar

Acknowledgements

Financial assistance and characterization facilities from Inter University Accelerator Centre (IUAC), New Delhi vide project no. IUAC/XIII.3A/62307 dated 11/08/2017 and thanks to Chemistry Department, Hanyang University Seoul Korea for providing Brainpool Fellowship to Dr. Ramphal Sharma. Also, the prolific discussion with Dr. Fouran Singh is gratefully acknowledged. Authors are also thankful to DST-FIST and UGC-SAP for their financial support.

Author information

Authors and Affiliations

Department of Physics, Dr. Babasaheb Ambedkar Marathwada University, Aurangabad, MS, 431004, India
Vishnu V. Kutwade, Avinash S. Dive, Makrand E. Sonawane & Ramphal Sharma

Department of Nanotechnology, Dr. Babasaheb Ambedkar Marathwada University, Aurangabad, MS, 431004, India
Ketan P. Gattu, Dipak A. Tonpe & Ramphal Sharma

Corresponding author

Correspondence to Ramphal Sharma.

Additional information

Publisher's Note

Rights and permissions

About this article

Cite this article

Kutwade, V.V., Gattu, K.P., Dive, A.S. *et al.* Enhanced photosensing by Mg-doped ZnO hexagonal rods via a feasible chemical route. *J Mater Sci: Mater Electron* 32, 6475–6486 (2021). https://doi.org/10.1007/s10854-021-05364-0

Received	Accepted	Published
16 October 2020	18 January 2021	12 February 2021

Issue Date
March 2021

DOI
https://doi.org/10.1007/s10854-021-05364-0

Share this article